Journal of Alloys and Compounds 509 (2011) 1716–1721

Contents lists available at ScienceDirect

Journal of Alloys and Compounds

journal homepage: www.elsevier.com/locate/jallcom

Characterization of zinc oxide nanoparticles synthesized by polymer assisted deposition method

R.C. Pawar, J.S. Shaikh, P.S. Shewale, P.S. Patil*

Thin Films Materials Laboratory, Department of Physics, Shivaji University, Kolhapur 416004, India

ARTICLE INFO

Article history:
Received 2 January 2010
Received in revised form 4 October 2010
Accepted 6 October 2010
Available online 14 October 2010

Keywords:
Zinc oxide nanoparticles
Polymer assisted deposition
TritonX100

ABSTRACT

Zinc oxide nanoparticles (ZNPs) are synthesized onto glass substrates by employing simple and low cost solution based modified polymer assisted deposition (PAD) method. Trionx100 is used as a capping agent and zinc acetate as the zinc source. TritonX100 concentration is varied from 0.02 to 0.45 M for the synthesis of pure ZnO NPs. TG–DTA analysis was employed to determine the decomposition temperature of TritonX100 and zinc acetate, which lead to the formation of ZnO. The films were further characterized by powder X-ray diffraction (XRD), scanning electron microscopy (SEM) and high-resolution transmission electron microscope (HR-TEM), Fourier transforms infrared spectroscopy (FT-IR) and room temperature photoluminescence (PL). The results indicate that the synthesized nanoparticles (NPs) exhibits the room temperature PL with two emission peaks, one corresponding to ZnO band edge emission and the other one to point defect states created due to oxygen deficiency. The first peak undergoes blue-shift due to change in NPs size while there is no shift in the second peak. Nevertheless, with increase in TritonX100 concentration the peak intensity of defect peak decreases, indicating that the highly pure NPs have been successfully synthesized by PAD method.

1. Introduction

Recently, the studies on use of polymers to synthesize metal-oxide based NPs of controlled size have gain momentum. Polymers enable active binding of metal ions present in the precursor that inhibit grain growth and hence facilitates production of NPs. Quantum size effects are observed in the particles, and the energy gap between the conduction and valence bands exhibits a blue-shift with decrease in particle size. Semiconductor particles that are in the nanometer size regime have attracted significant attention because of their atom-like size dependent properties [1]. The crystallization inorganic material in the presence of polymers has been efficient method to obtain composite materials. Two different aspects are combined; first, polymers can act as template and second is polymer controlled crystallization. Among the various nanomaterials ZnO, with direct wide band gap energy of 3.37 eV and a large exciton binding energy (60 meV), has become one of the most important functional materials with unique properties of near-ultraviolet emission, optical transparency, electric conductivity and piezoelectricity [2,3]. These ZNPs have new exciting properties and wide technological applications such as photocatalysis, chemical remediation, photoinitiation of polymerization reactions, quantum dot devices and solar energy conversion. Furthermore, it is well known that low-dimensional structures may have superior optical properties over bulk material due to the quantum confinement effect. These days, the focus is moving on to the synthesis of ZnO nanostructures. The techniques used for synthesizing ZnO nanostructures mainly include templated growth [4], patterned catalytic growth [5], substrates-induced vapor deposition [6], solution-phase deposition [7], electrochemical route [8] and chemical reaction [9]. These methods require high temperature, expensive substrates, high cost, tedious procedures, sophisticated equipments and rigorous experimental conditions, which can be called 'noble' methods. Hence it is necessary to find out a simple and low cost method to synthesize ZnO nanostructures to tackle the problems. In view of this, we followed a simple, inexpensive, environmentally benign, solution-based method with some modification to produce NPs without templates and catalysts [10].

In the present work we report the synthesis of ZNPs by PAD method. TritonX100 is used as a capping agent. Films are prepared by drop-casting the TX and zinc acetate prepared solution on to glass substrates and annealed at 400 °C for 5 h in air. Annealed films are used for further characterizations.

2. Experimental

The ZNPs synthesized in this work are deposited onto glass substrates using the following procedure. The 0.1 M zinc acetate dihydrate was added into 4 ml deionized water at room temperature. Subsequently, 0.02 M polyethylene glycol-p-isooctylphenyl ether [TritonX100, TX] was added into the solution and 1 ml of

* Corresponding author. Tel.: +91 231 2609229; fax: +91 231 2691533.
E-mail address: psp_phy@unishivaji.ac.in (P.S. Patil).

0925-8388/$ – see front matter © 2010 Elsevier B.V. All rights reserved.
doi:10.1016/j.jallcom.2010.10.019

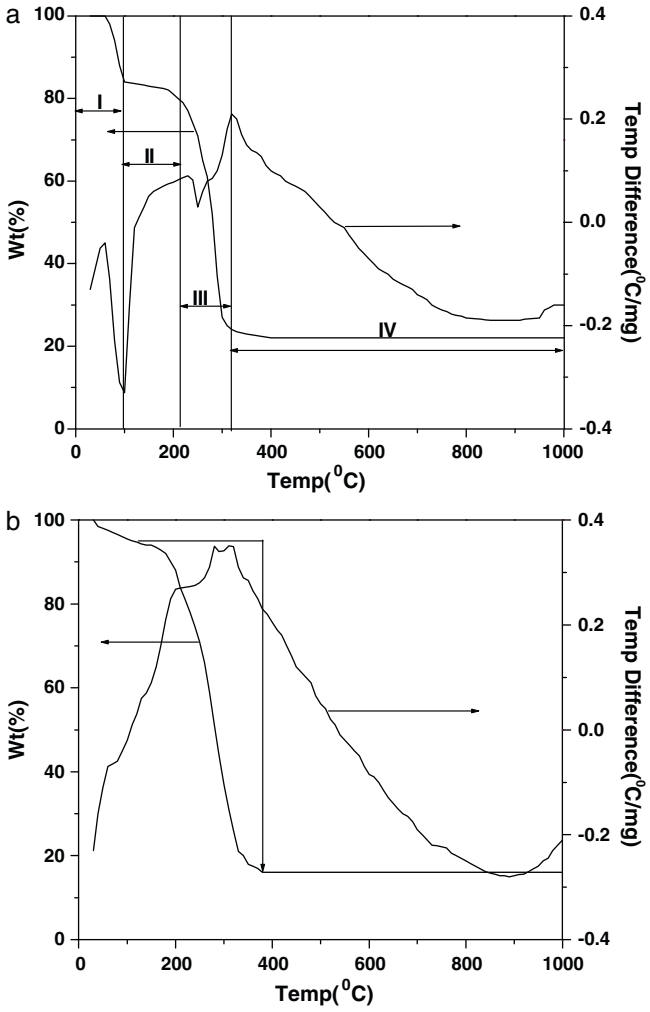

Fig. 1. (a) TG–DTA curves for studying decomposition behavior of zinc acetate dihydrate [$Zn(CH_3COO)_2{\cdot}2H_2O$] and (b) mixture of zinc acetate and TritonX100 in air atmosphere.

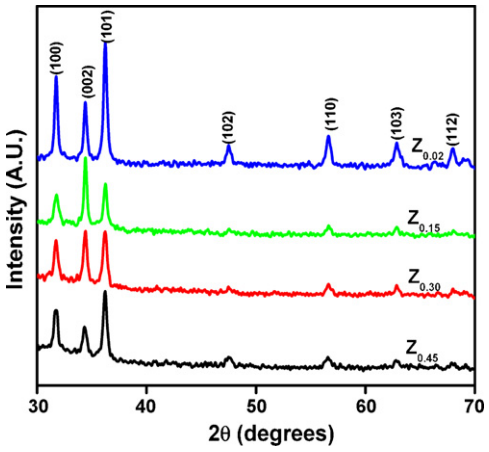

Fig. 2. XRD patterns of the $Z_{0.02}$, $Z_{0.15}$, $Z_{0.30}$ and $Z_{0.45}$ samples.

3. Results and discussion

The thermogram recorded for zinc acetate (Thomas Baker, 99.5%) powder is shown in Fig. 1(a). The thermal evolution in oxygen ambient takes place in four consecutive stages with weight losses for which the inflection point coincides with the temperature corresponding to the endotherms and exotherms in DTA trace. The weight loss of precursor zinc acetate [$Zn(CH_3COO)_2{\cdot}2H_2O$] begins at 60 °C. Initially, weight loss of 16.43% of zinc acetate in the temperature range of 60–100 °C was observed (Step I).This is indicated by the endothermic peak at 95 °C due to the evaporation of physisorbed water from the precursor. This is followed by a slow decay of TGA curve in the temperature range of 100–240 °C (Step II). The rapid decay in TGA curve was takes place during 240–300 °C (Step III). During step II & III; total weight loss was 60.15%. These consequent weight losses are attributed to the decay leading to the decomposition of acetate groups. A further weight loss at the temperature of 300 °C coincides with an exothermic peak indicating the formation of ZnO phase and becomes stable after the temperature of 400 °C. After 400 °C the TGA trace is stable with no further weight loss indicating the decomposition of zinc acetate formation of stable ZnO phase. In the DTA trace, the exothermic peak signifies the crystallization or phase formation [11].

For the first endothermic peak,

$$Zn(CH_3COO)_2 \cdot 2H_2O \xrightarrow{\Delta} Zn(CH_3COO)_{2\,liq.} + 2H_2O_{vapor} \uparrow \text{(Physisorbed water)}$$

For the second endothermic peak,

$$Zn(CH_3COO)_{2\,liq.} + 2H_2O_{liq.} \xrightarrow{\Delta} Zn(CH_3COO)_{2\,solid} + 2H_2O_{vapor} \uparrow \text{(Chemisorbed water)}$$

For the exothermic peak

$$Zn(CH_3COO)_{2\,solid} \xrightarrow[\text{Oxidation}]{\Delta} ZnO_{solid} + 2(CH_3COO) \uparrow + 2(CH_3) \uparrow + 2(CO_2) \uparrow$$

TG–DTA curve of TX + zinc acetate sample is shown in Fig. 1(b). Here the thermal evolution in O_2 atmosphere takes in three consecutive stages with weight losses. In first stage, there was minor weight loss of 0.09% of sample observed in the temperature range 30–150 °C. In second stage, rapid weight loss of 73.61% of sample takes place in the temperature range 150–390 °C and this is due to decomposition of both zinc acetate and TX. Finally, above 390 °C the thermally stable phase is observed. In case of DTA trace, there were two broad exothermic peaks observed, which are due to crystallization of the sample.

Fig. 2 shows XRD spectra of the samples prepared by varying TX concentration. All the samples are polycrystalline with peaks corresponds to the wurtzite ZnO [JCPDS card No. 36–1451, $a = 3.2501$ Å, $c = 5.2071$ Å, space group: $P6_3mc(1\,8\,6)$] with a good crystallinity.

acetone was further added. Finally this solution was drop-casted on to the cleaned glass substrates. The samples were dried at room temperature over night. Dried samples were annealed in air at 400 °C for 5 h. TritonX100 concentration is varied as; 0.02, 0.15, 0.30 and 0.45 M, and the samples are denoted as $Z_{0.02}$, $Z_{0.15}$, $Z_{0.30}$ and $Z_{0.45}$, respectively.

The samples were characterized by means of structural, electrical and optical techniques. To select the range of annealing temperature for formation of NPs, thermo gravimetric analysis (TGA) and differential thermal analysis (DTA) of zinc acetate was carried out using TA instrument (USA) STD 2960. The phase formation was examined by using a powder XRD Philips PW3710 with Cu Kα ($\lambda = 1.54056$ Å) radiation operating at 40 kV and 30 mA. The morphological features of NPs were studied by using SEM, JEOL JSM 6360, secondary electron imaging. HR-TEM measurement was carried out on JEOL make 3010 Model at 300 kV. The UV–vis absorption spectra were recorded on a [systronics-119 model] spectrophotometer. The powder scratched from deposited films was characterized by FT-IR spectroscopy using PerkinElmer IR spectrometer model 783 in the spectral range 450–4000 cm^{-1}. To record IR patterns, the pellets were prepared by mixing KBr with NPs powder collected by scratching the films from glass substrates and then pressing powder between two pieces of polished steel. The room temperature photoluminescence was recorded by using an excitation wavelength of 320 nm on a UV–vis single beam Spectroflourometer [JASCO 750, Japan].

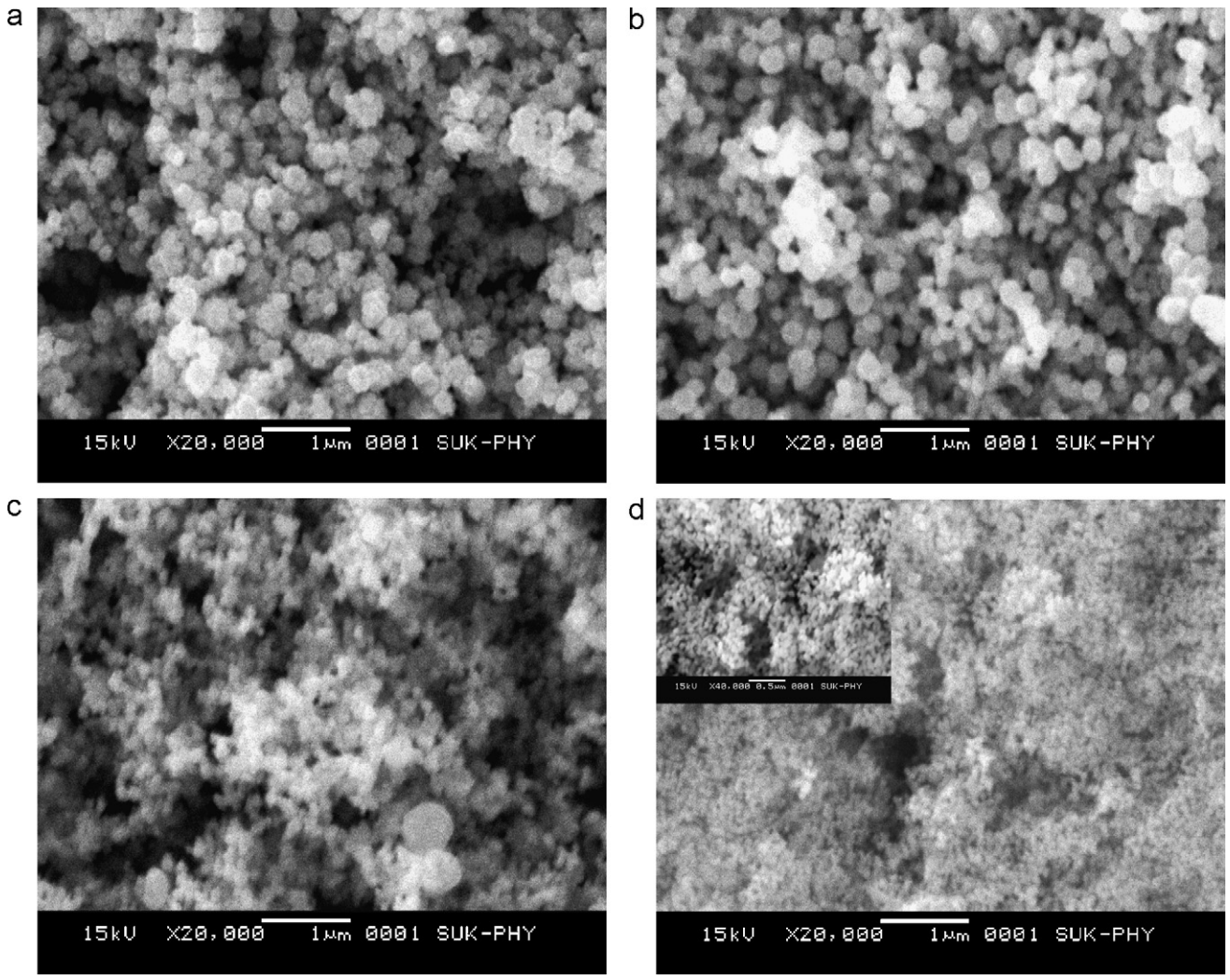

Fig. 3. SEM images of the $Z_{0.02}$, $Z_{0.15}$, $Z_{0.30}$ and $Z_{0.45}$ samples. All the images are recorded at ×20,000 magnification. Inset shows the magnified image of $Z_{0.45}$ sample.

No further characteristic peaks of impurities, such as $Zn(OH)_2$ observed. The crystallite's size (t) was deduced from well-known Scherer's formula,

$$t = \frac{0.9\lambda}{\beta \cos(\theta)} \quad (1)$$

where t = crystallite size in nm, λ = wavelength of X-ray incident on sample, β = Full width half maxima and θ = angle at which maximum peak observed. The variation in crystallite's size with concentrations of TX is given in Table 1. It is observed that the crystallite size decreases with increase in concentration of TX in the solution. All the samples exhibit peaks along (1 0 0), (0 0 2), (1 0 1), (1 0 2), (1 1 0), (1 0 3) and (1 1 2) plane. Moreover, the peaks become broader with the increment in TX.

The PAD deposited ZnO samples were analyzed by SEM to determine the influence of TX on the morphology. The change in NPs size is revealed for the samples deposited at various TX concentrations. Changes in sample morphology with the TX are observed. Well-defined grains of about 230 nm are obtained for the $Z_{0.02}$ sample (Fig. 3(a)). With an increase in TX above 0.02 M, the sample morphologies change substantially and highly dispersed NPs are formed for $Z_{0.15}$ Fig. 3(b). Further increment in TX, particles size becomes smaller (Fig. 3(c)). The decrement in the average grain size up to 60–70 nm (Fig. 3(d)) is on account of the effect of TX that causes growth of the grains. Fig. 4 shows the HR-TEM image of $Z_{0.45}$ sample with SAED pattern. The TEM image reveals that the particles with average 25 nm in diameters showing the samples are nanocrystalline in nature. The most of the particles are randomly oriented. The circular bright and dark fringes in SAED pattern confirm the NPs are polycrystalline.

Fig. 5 shows the IR spectra of pure TX and ZNPs with different concentration of TX. The intense broad band for each sample in

Table 1
The values of crystallite size, TX concentrations, bandgap energy and PL peaks in UV and visible region.

Sample name	TritonX100 conc. (M)	Crystallite size (nm)	Band gap energy (eV)	PL peaks	
				Band edge peak (eV)	Defect peak (eV)
$Z_{0.02}$	0.02	18	3.15	3.08	2.63
$Z_{0.15}$	0.15	17	3.18	3.10	2.63
$Z_{0.30}$	0.30	16	3.21	3.15	2.63
$Z_{0.45}$	0.45	11	3.24	3.23	2.63

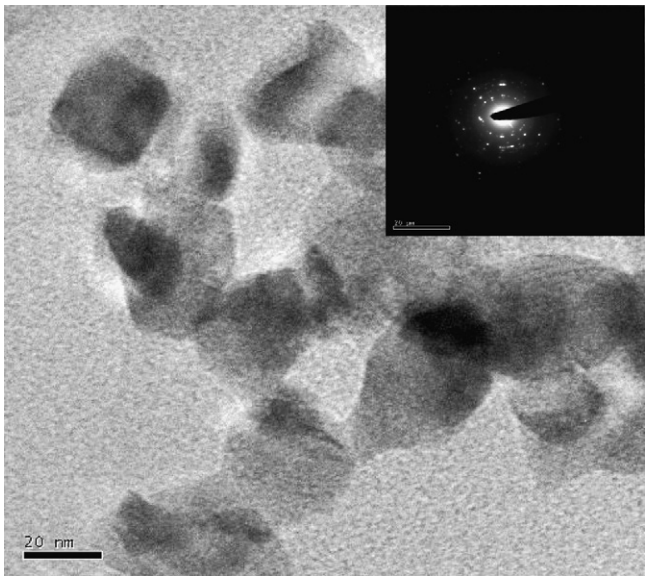

Fig. 4. HRTEM image of the $Z_{0.45}$ sample. Inset shows the SAED pattern.

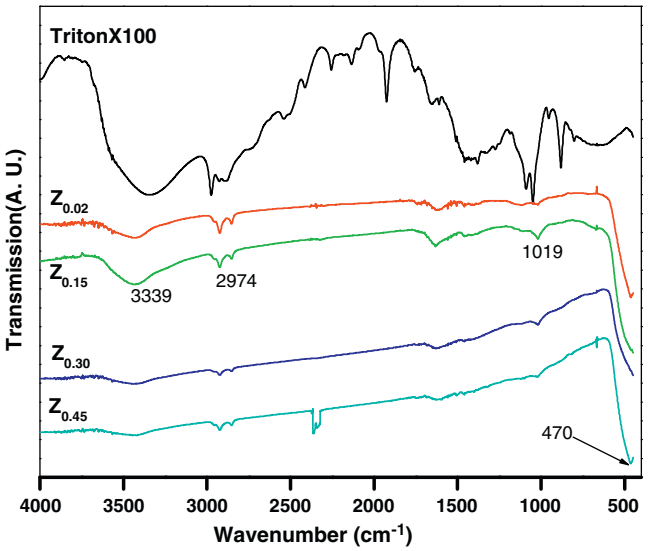

Fig. 5. IR transmittance spectra of the $Z_{0.02}$, $Z_{0.15}$, $Z_{0.30}$ and $Z_{0.45}$ sample recorded in the wave number range of 450–4000 cm^{-1}.

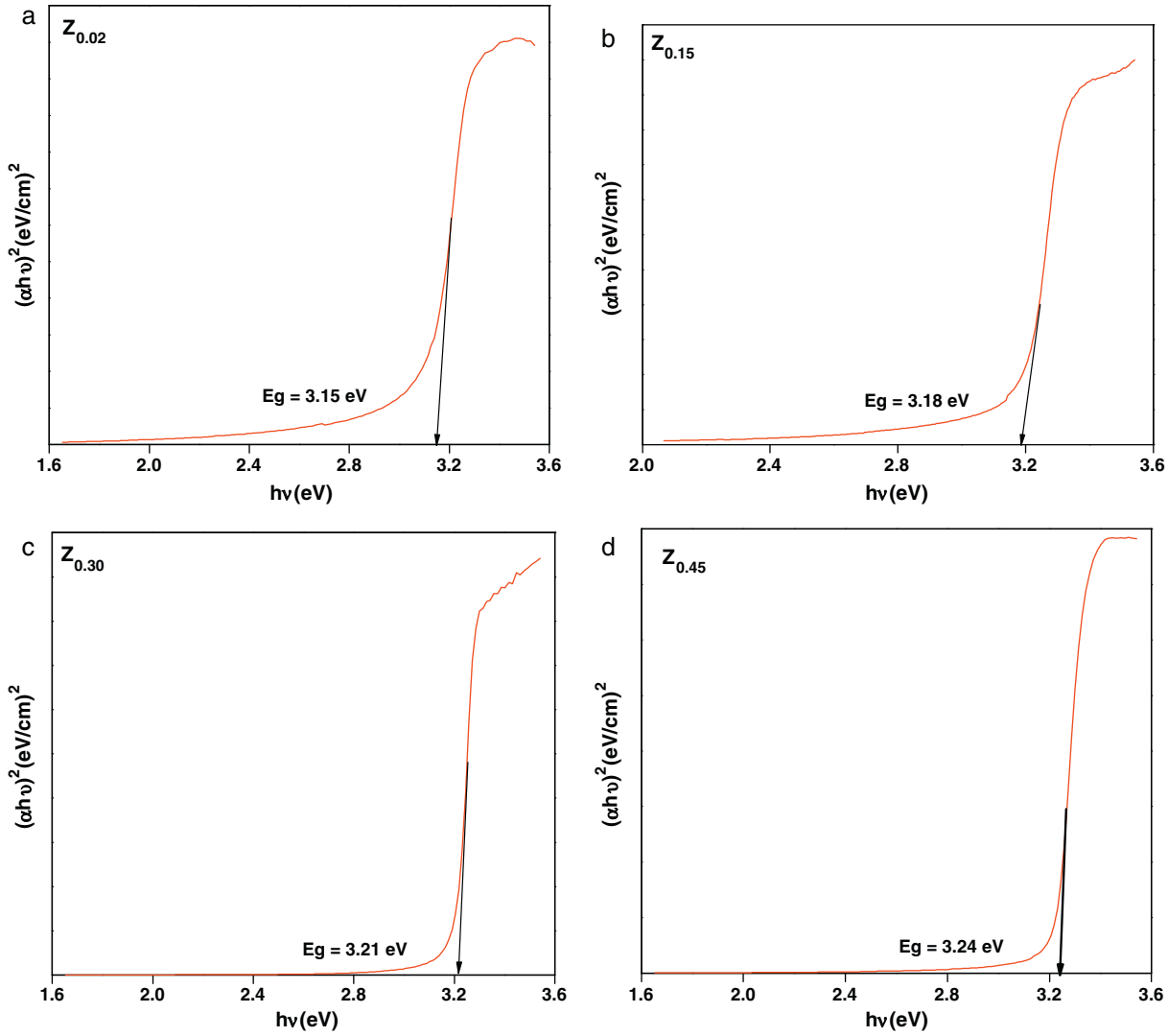

Fig. 6. Optical bandgap spectra of the $Z_{0.02}$, $Z_{0.15}$, $Z_{0.30}$ and $Z_{0.45}$ samples in the energy range between 1.6 and 3.6 eV.

the range of 470–534 cm^{-1} due to the vibrational property of ZnO nanocrystals [12]. The remaining peaks at 3339 and 2974 cm^{-1} in sample are assigned to the vibrations of –OH and $–CH_2$ groups of TX, respectively [13]. The broad peak at 1019 cm^{-1} relate to complex structure of the ZNPs and TX as explained by Du et al. [14]. The spectrum of pure TX recorded for comparison. In spite of complete washing of the final product, the IR spectra recorded the peaks corresponding to TX, indicating the strong interactions of TX with the ZNPs. Hence the IR spectra reveal that the samples are composite of ZNPs with few percentage of TX.

The Optical absorption in the UV–vis region is dominated by the optical band gap (E_g) of the semiconductor that is related to the optical absorption coefficient (α) and the incident photon energy ($h\nu$) by the relation $\alpha = (E_g - h\nu)^n$, where 'n' depends on the kind of optical transition that prevails. Specifically, n is 1/2, 3/2, 2 and 3 when the transition is direct-allowed, direct-forbidden, indirect-allowed, and indirect-forbidden respectively. ZnO is a direct-allowed band gap semiconductor; hence graph is plotted α^2 versus photon energy as a function of TX concentration. The direct-allowed E_g estimated from the plot is varied ranging from 3.15 to 3.24 eV. The change in optical band gap is observed due to variation in concentration of TX from 0.02 to 0.45 M. Hence as the TX concentration increases the crystallite size of NPs decreases. This observation reveals a blue shift of band gap energy with increment in TX concentration relative to bulk ZnO (380 nm) [15]. The increased band gap is attributed to quantum size effect (QSE).

A single band model has been widely used to discuss the QSE of the energy band gap in semiconductor NPs. Considering the infinite potential barrier at the interface of NPs and surrounding material, Brus has calculated the broadened band gap energy due to QSE [16,17]. However, the calculated band gap energy using Brus model is higher than the actual. To overcome the limitation of Brus model, Nosaka has suggested a new model using the finite potential barrier. The band gap energy given by Nosaka model is [18],

$$E_{opt}(R) = E_{bulk} + E_o\left[\frac{a+b}{(E_o m_e^*/m_o)^{1/2}R + c}\right] + E_o\left[\frac{a+b}{(E_o m_h^*/m_o)^{1/2}R + c^2}\right] - \frac{1.786e^2}{(4\pi\varepsilon_o\varepsilon_r R)} \quad (2)$$

where E_o is the finite potential energy barrier. The energy gap of bulk ZnO is 3.2 eV. The constant parameters a, b, and c depend on the charge carriers' effective masses, R is the particles radius. These parameters are given by Nosaka in plots of the relationship between the parameters and the effective mass ratios m_e^*/m_o and m_h^*/m_o. Many researchers are observed that the calculated band gap energy using Nosaka model is well matches with the experimentally predicted value [19]. The band gap energy of the ZNPs was significantly increased with decreasing the crystallite size from 18 to 11 nm. Band-edge absorption spectra features indicate narrow size distribution of the NPs [20,21]. The crystalline quality of a semiconductor has been related to the appearance of sharp edge in its optical absorption [22] (Fig. 6).

Fig. 7 shows that the room temperature PL spectra of $Z_{0.02}$, $Z_{0.15}$, $Z_{0.30}$ and $Z_{0.45}$ samples. The characteristic UV (384 nm, 3.23 eV) and visible (471 nm, 2.63 eV) peaks are observed due to high exciton energy and direct band gap of ZnO. The UV emission in ZnO has been well documented and discussed by many researchers in the literature [23,24]. It is attributed to near band edge transition processes arising from energy loss due to a strong electron-phonon interaction at room temperature [25]. The visible emission in ZnO is far from clear. It has been investigated that different extrinsic and intrinsic defect centers are responsible for green, yellow, and red emissions. Extrinsic lattice defect produce impurity energy levels in the band gap of ZnO, which is one of the reason for visible emission. Intrinsic defect such as, oxygen vacancies (V_o), zinc vacancies (V_{Zn}), oxygen interstitials (O_i), zinc interstitials (Z_{ni}), and oxygen antisites

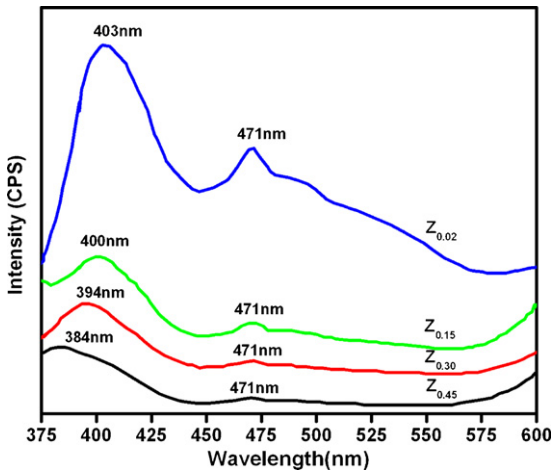

Fig. 7. The room temperature PL spectra with an excitation wavelength 320 nm of the $Z_{0.02}$, $Z_{0.15}$, $Z_{0.30}$ and $Z_{0.45}$ samples.

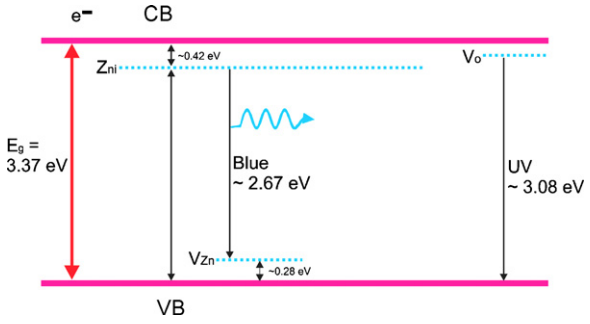

Fig. 8. Schematic illustration of the ZnO band structure and the proposed band edge emission and blue–green emission.

(O_{Zn}) are responsible for visible PL [26]. Bacsa et al. have shown that the point defect such as Zni in combination with surface defects causes the green emission. Yellow and red emissions are attributed to the defects of interstitial oxygen and zinc, respectively [27]. Blue emission is attributed to the transition of electron from donor Z_{ni} level to neutral acceptor V_{zn} level [28]. In present work, although both UV and visible emission are present in all samples, their intensities change observed for the band-edge as well as visible band. TX affects on the PL property of ZNPs. For $Z_{0.02}$ sample the both peaks are highly intense and broad. For the $Z_{0.15}$, $Z_{0.30}$ and $Z_{0.45}$ samples, emission of band edge and blue peaks are merged compare to $Z_{0.02}$, due to the capping of TX to ZNPs. The band edge peak is shifted towards the higher energy as TX concentration increases due to decrease in crystallite size.

Fig. 8 schematically depicts the positions of the possible defect levels in the samples and it seems that the emission at 403 nm (3.08 eV) can be assigned to the recombination of electrons at minima of conduction band and holes at V_{Zn} above valence band. The blue emission is due to the recombination of electrons at V_{Zi} and holes at the maxima of the valence band V_{Zn} [29–31].

4. Conclusions

In summary, ZnO nanoparticles have been successfully synthesized on to the glass substrates by a simple and cost effective polymer assisted deposition method. The preparative parameters were fine tuned to yield monodispersed ZnO nanoparticles.

The structural, optical and morphological features of ZnO samples are dependent on TritonX100 concentration. The HR-TEM shows that the samples are nanocrystalline with average 25 nm size. The obtained IR spectra give the samples are composite of ZnO nanoparticles with few percentage of TX. The synthesized NPs exhibit blue–green emission at room temperature.

Acknowledgments

One of the authors Mr. R.C. Pawar is thankful to University Grants Commission, New Delhi, for awarding the "Research Fellowship in Science for Meritorious Students to Promote Quality Research in Universities" under the UGC-DRS (SAP)–II programme. Authors are also thankful to Prof. G.U. Kulkarni, JNCASR, India for providing HRTEM facility.

References

[1] S. Norifusa, N. Toshio, K. Kenta, Y. Kimihisa, Nat. Nanotechnol. 3 (2008) 106–111.
[2] P.F.W. Simon, R. Ulrich, H.W. Spiess, U. Wiesner, Chem. Mater. 13 (2001) 3464–3486.
[3] S.H. Yu, H. Colfen, J. Mater. Chem. 14 (2004) 2124–2147.
[4] U. Pal, P. Santiago, J. Phys. Chem. B 109 (2005) 15317–15321.
[5] M.H. Huang, S. Mao, H. Feick, H.Q. Yan, Y.Y. Wu, H. Kind, E. Weber, Science 292 (2001) 1897–1899.
[6] J.J. Wu, S.C. Liu, Adv. Mater. 14 (2002) 215–218.
[7] A.I. Inamdar, S.H. Mujawar, P.S. Patil, Int. J. Electrochem. Sci. 2 (2007) 797–808.
[8] L. Vayssieres, K. Keis, A. Hagfeldt, S.E. Lindquist, Chem. Mater. 13 (2001) 4395–4398.
[9] H. Zhang, D.R. Yang, X.Y. Ma, D.L. Que, J. Phys. Chem. B 109 (2005) 17055–17059.
[10] Q.X. Jia, T.M. Maccleskey, A.K. Burrell, Y. Lin, G.E. Collis, H. Wang, A.D.Q. Li, S.R. Foltyn, Nat. Mater. 3 (2004) 529–532.
[11] G.R. Chatwal, S.K. Anand, Instrumental Methods of Chemical Analysis, Himalaya Publishing House, 2006.
[12] N. Vigneshwaran, S. Kumar, A.A. Kathe, P.V. Varadarajan, V. Prasad, Nanotechnology 17 (2006) 5087–5095.
[13] Y. Zheng, C. Chen, Y. Zhan, X. Lin, Q. Zheng, K. Wei, J. Zhu, Y. Zhu, Inorg. Chem. 46 (2007) 6675–6682.
[14] X.W. Du, Y.S. Fu, J. Sun, X. Hanm, J. Liu, Semicond. Sci. Technol. 21 (2006) 1202–1206.
[15] V. Prasad, C.D. Souza, D. Yadav, A.J. Shaikh, N. Vigneshwaran, Spectrochim. Acta A 65 (2006) 173–178.
[16] L.E. Brus, J. Chem. Phys. 79 (1983) 5566–5571.
[17] L.E. Brus, J. Chem. Phys. 80 (1983) 4403–4409.
[18] Y. Nosaka, J. Phys. Chem. 95 (1991) 5054–5058.
[19] H. Usui, S. Abe, S.J. Ohnuma, J. Phys. Chem. C 113 (2009) 20589–20593.
[20] Y. Zao, H.L. Quan, C.Y. Hong, Z. Binsuo, Y.G. Wang, T.H. Wang, Nanotechnology 19 (2008) 035704–035708.
[21] T. Yoshinda, M. Tochimotom, D. Schlettwein, D. Wohrle, T. Sugiura, H. Minoura, Chem. Mater. 11 (1999) 2657–2667.
[22] W. Chen, Z.J. Lin, Z.G. Wang, L.Y. Lin, Solid State Commun. 100 (1996) 101–104.
[23] K.H. Tam, C.K. Cheung, Y.H. Leung, A.B. Djurisic, C.C. Ling, C.D. Beling, S. Fung, W.M. Kwok, W.K. Chan, D.L. Phillips, L. Ding, W.K. Ge, J. Phys. Chem. B 110 (2006) 20865–20871.
[24] R.R. Bacsa, J.D. Ghys, M. Verelst, A. Falqui, B. Machado, W.S. Bacsa, P. Chen, S.M. Zakeeruddin, M. Graetzel, P. Serp, Adv. Funct. Mater. 19 (2009) 875–886.
[25] H. Usui, J. Phys. Chem. C 111 (2007) 9060–9065.
[26] L.S. Mende, L. Judith, M. Driscoll, Mater. Today 10 (2007) 40–48.
[27] S. Dutta, S. Chattopadhyay, A. Sarkar, M. Chakrabarti, D. Sanyal, D. Jana, Prog. Mater. Sci. 54 (2009) 89–136.
[28] Y.Y. Tay, T.T. Tan, M.H. Liang, F. Boey, S. Li, Phys. Chem. Chem. Phys. 12 (2010) 6008–6013.
[29] H. Hecht, E. Mollwo, Solid State Commun. 9 (1971) 2167–2171.
[30] L.M. Wang, L. Gao, J. Mater. Chem. 13 (2003) 2551–2554.
[31] Z.L. Wang, P.X. Gao, S. Song, J. Liu, Adv. Mater. 19 (2006) 67–72.